

# Electron Conductive and Transparent Hydrogels for Recording Brain Neural Signals and Neuromodulation

Quanduo Liang, Zhenzhen Shen, Xiguang Sun, Dehai Yu, Kewei Liu, Samuel M. Mugo, Wei Chen, Dong Wang,\* and Qiang Zhang\*

Recording brain neural signals and optogenetic neuromodulations open frontiers in decoding brain neural information and neurodegenerative disease therapeutics. Conventional implantable probes suffer from modulus mismatch with biological tissues and an irreconcilable tradeoff between transparency and electron conductivity. Herein, a strategy is proposed to address these tradeoffs, which generates conductive and transparent hydrogels with polypyrrole-decorated microgels as cross-linkers. The optical transparency of the electrodes can be attributed to the special structures that allow light waves to bypass the microgel particles and minimize their interaction. Demonstrated by probing the hippocampus of rat brains, the biomimetic electrode shows a prolonged capacity for simultaneous optogenetic neuromodulation and recording of brain neural signals. More importantly, an intriguing brain-machine interaction is realized, which involves signal input to the brain, brain neural signal generation, and controlling limb behaviors. This breakthrough work represents a significant scientific advancement toward decoding brain neural information and developing neurodegenerative disease therapies.

direct communication between the brain and external devices by capturing neuronal activity.<sup>[6–11]</sup> Optogenetics is one of the main neuromodulations which utilizes external optical signals to modulate brain neural circuits and trigger correspondent physiological behaviors.<sup>[12–18]</sup> It is intriguing to understand how the external triggers stimulate brain neural circuitry and establish the correlation between brain neural signals and physiological behaviors. Thus, it is essential to record the brain's neural signals during external optical stimulation. The recording performance of these probes is largely dependent on the inherent properties of corresponding materials, especially mechanical modulus, conductivity, and transparency. For example, conductive and transparent hydrogels were developed using a mechanically interlocked supramolecular structure, which shows the capability of recording stable electromyography

## 1. Introduction


Emerging studies on brain neural circuits seek to reveal the origin of human behaviors and thoughts. Through the science of neuromodulations, these studies also support the diagnostics and therapeutics of brain disorders and neurodegenerative diseases such as Alzheimer's disease, Parkinson's disease, and mental illnesses.<sup>[1–5]</sup> Brain neural circuit studies have triggered the exploration of the futuristic brain-computer interface that can generate

(EMG) signals and performing localized neuromodulation for controlling rat behaviors.<sup>[19]</sup> The mechanically interlocked supramolecular structure allows high stretchability, meanwhile, creates large conformational freedom reducing  $\pi$ - $\pi$  stackings between PEDOT backbones and resulting in high optical transparency. In another case, a stretchable, neurochemical interface was prepared by immobilizing laser-induced graphene nanofiber networks in a polystyrene-*block*-poly(ethylene-*ran*-butylene)-*block*-polystyrene elastomer.<sup>[20]</sup> The stretchable neurochemical

Q. Liang, Z. Shen, W. Chen, Q. Zhang  
State Key Laboratory of Electroanalytical Chemistry  
Changchun Institute of Applied Chemistry  
Chinese Academy of Sciences  
Changchun 130022, P. R. China  
E-mail: qiang.zhang@ciac.ac.cn

Q. Liang, Z. Shen, W. Chen, Q. Zhang  
School of Applied Chemistry and Engineering  
University of Science and Technology of China  
Hefei 230026, P. R. China

X. Sun, D. Yu  
Department of Hand Surgery  
Public Research Platform  
The First Hospital of Jilin University  
Changchun 130061, P. R. China

 The ORCID identification number(s) for the author(s) of this article can be found under <https://doi.org/10.1002/adma.202211159>.

K. Liu  
State Key Laboratory of Luminescence and Applications  
Changchun Institute of Optics  
Fine Mechanics and Physics  
Chinese Academy of Sciences  
Changchun 130033, P. R. China

S. M. Mugo  
Department of Physical Sciences  
MacEwan University  
Edmonton ABT5J4S2, Canada

D. Wang  
Key Laboratory of Biomedical Engineering of Hainan Province  
School of Biomedical Engineering  
Hainan University  
Haikou 570228, China  
E-mail: wangdong@hainanu.edu.cn

DOI: 10.1002/adma.202211159

interface was used for chronic in vivo monoamine sensing in the brain of behaving rats. Although some achievements have been realized by scientists, materials used to make the implantable probes suffer from several challenges such as a mismatch in chemo-mechanical properties and a tradeoff between electron conduction and optical transparency.<sup>[21,22]</sup>

Due to their inherently high electronic conductivity and electrochemical stability, traditional implantable probes are primarily fabricated using inorganic materials. However, the inorganic electrodes show an extremely high elasticity modulus, for instance, >100 MPa for platinum, which is much higher than that of human tissues (10–100 kPa).<sup>[23,24]</sup> When a rigid electrode is implanted into a brain to record neural signals, with time the electrode will be covered by glial cells, which would attenuate brain neural signals from blocking electron transfer.<sup>[25]</sup> The mismatch in the mechanical property between the rigid materials and biological tissues would lead to micromotion during long-term implantation resulting in neural tissue damage and concomitant foreign body responses.<sup>[26]</sup> Moreover, the metal-based neural electrodes produce interfering light-induced artifacts due to the small energy band gap of metals (e.g., iridium, gold, and platinum), which increases signal noises and false results.<sup>[27,28]</sup> The flexible probes can be prepared by depositing a thin metal or metal oxide layer on a polymer substrate or composites of flexible polymers with carbon materials or conductive polymers.<sup>[29–32]</sup> Although the literature has reported flexible sensors with a modulus of below 100 MPa, they are still much more rigid compared to neural tissues.<sup>[33,34]</sup> To resolve the issue of mechanical property mismatch between implantable materials and neural tissues, hydrogels have attracted attention due to their excellent biocompatibility. Hydrogels have a water-rich 3D structure that can imitate the chemo-mechanical properties of neural tissues. Thus, hydrogels have been utilized as neural interfaces for optical waveguides and neural electrodes. For example, Zhao and co-workers developed a multifunctional probe by integrating multiple fibers into a soft hydrogel matrix that simulates brain tissue for electrophysiological, optogenetic, and behavioral studies of neural circuits.<sup>[35]</sup> Cullen and co-workers prepared living electrodes by coating cortical neurons with agarose hydrogels to monitor and modulate brain activity.<sup>[36]</sup> Silk protein hydrogels cross-linked by poly(ethylene glycol) diglycidyl ether have been successfully demonstrated for the in situ recording of the neural activity of rat brains by Chen and co-workers.<sup>[37]</sup> Although hydrogels show good biological compatibility and reduce the mechanical discrepancy between electrodes and brain tissue, they still suffer from poor conductivity, signal attenuation, low optical transmission, and swelling that hinder their applications in recording neural signals and neuromodulation. The conventional remedy is to achieve a good conductivity performance by incorporating ions or conductive fillers into hydrogel networks.<sup>[38]</sup> However, the free ionic electrolytes can diffuse from the hydrogel networks into tissues, resulting in a decrease in conductivity and loss in performance during long-term implantable applications. Stable electron conduction can be realized by utilizing conductive fillers such as metal nanoparticles, conducting polymers, and carbon materials. However, due to the dark color features of conductive fillers, the corresponding composite hydrogels are opaque and do not lend well to light input for brain

activity modulation. Moreover, the high content of conductive fillers increases the modulus of the composite hydrogels while decreasing their flexibility, thereby causing mechanical discrepancy and adverse biological responses.

Consequently, two scientific issues should be resolved to prepare superior implantable probes capable of simultaneous neuromodulations and recording brain neural signals. We propose hybrid implantable probes that can dually address: 1) the tradeoff between matched modulus and electron conductivity; 2) the tradeoff between transparency and electron conductivity. Herein, we utilize the Tyndall effect to solve the transparent performance issue and hydrogel electron conductivity. Tyndall effect postulates that when the size of nanoparticles is smaller than the wavelength of visible light (400–800 nm), the optical wave bypasses these nanoparticles with minimal radiation interaction. In this work, microgels (diameter: 200 nm) were used as carriers for conductive polypyrrole (PPy), which were incorporated in hydrogels to promote optical transparency meanwhile maintaining good electron conductivity. In addition, the microgels served as cross-linking centers in the hydrogel networks to generate low modulus, high flexibility, and good electron conductivity. The microgels were connected with the hydrogel networks by supramolecular interaction rather than covalent bonds. When the hydrogels were subjected to a stretching or compression process, the mechanical force can be transferred to the microgels resulting in a reversible deformation. Compared with small molecular cross-linkers and other rigid nanoparticles such as Au nanoparticles, the microgels function as a mechanical buffer with matching mechanical properties similar to the brain neural tissues, hence ensuring the hydrogels have good biocompatibility and negligible foreign body response. We further demonstrate the sensing applications of the hydrogels as wearable and implantable sensors in various scenarios (**Figure 1**). 1) The hydrogels show high sensitivity and large detection ranges as strain sensors. 2) The hydrogels were used to record physiological signals such as vocal cords vibration, electrocardiogram (ECG), and electromyogram (EMG). 3) The hydrogel-based electrodes show the capability of recording local field potentials (LFPs) when implanted in the hippocampus CA1 region of rat brains, yielding more stable signals with larger amplitude compared to ion conductive hydrogel electrodes during 8 weeks of implantation testing. 4) As a proof-of-concept of optogenetic neuromodulations, the hydrogel electrodes were successfully used to investigate the animal behavior and synchronous brain neural signals in response to the external optical input. To the best of our knowledge, it is the first time the correlation between brain neural signals in the primary motor cortex region and corresponding limb behaviors modulated by light stimulation is established. This work validates the following advancements for implantable brain probes: 1) a new strategy to address the tradeoff between transparency and electron conductivity; 2) the supramolecular structure design of hydrogels which overcomes the tradeoff between matched modulus and electron conductivity; 3) stable and continuous brain signals recording using the prepared implantable probes for 8 weeks; and 4) optical stimulation of the brain via the hydrogel electrode and simultaneous monitoring of the resultant brain neural signals with negligible influence of photoelectric artifacts, thereby understanding neurological behaviors.

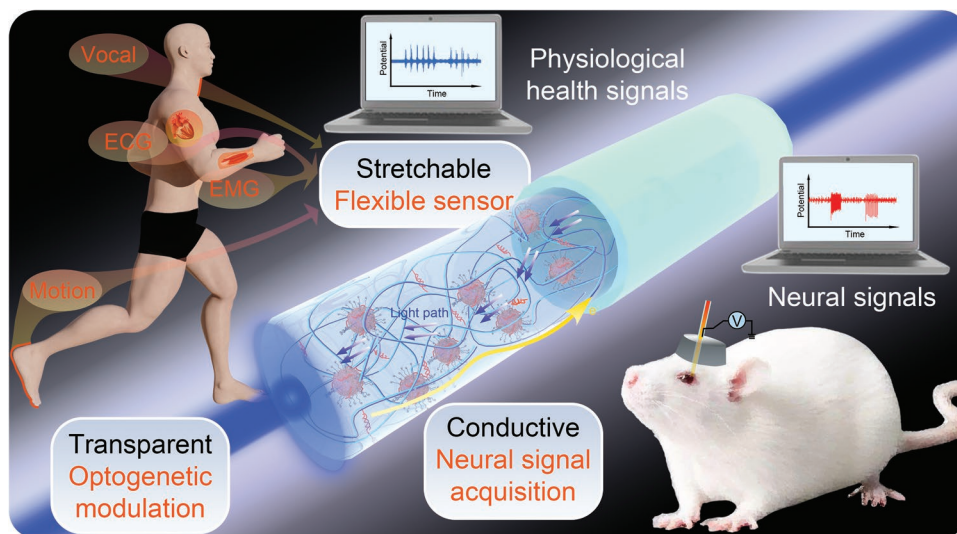


**Figure 1.** Schematic diagram of the hydrogel structure and its applications as wearable and implantable sensors.

## 2. Results and Discussions

### 2.1. Preparation and Characterization of Hydrogels

The conductive microgels were prepared by integrating PPy on the surface of microgels, as shown in **Figure 2a**. Initially, the microgels were synthesized by the precipitation copolymerization of *N*-isopropylacrylamide, *N,N'*-methylenebisacrylamide, and acrylic acid. Subsequently, PPy formed on the surface of microgels through the in situ polymerization of pyrrole. The carboxylic acid groups of the microgels can interact with pyrrole to facilitate the distribution of pyrrole monomers around poly(*N*-isopropylacrylamide) chains and form an interpenetrating polymer chain structure. The microgels were designated as PM-*X*, where *X* is the mass percentage of PPy in the microgels measured by thermogravimetric analysis (Table S1, Supporting Information). The microgels were characterized by Fourier transform infrared spectra (Figure S1, Supporting Information) and transmission electron microscope (Figure 2b–d and Figure S2, Supporting Information). As shown in Figure 2b–d, clear small PPy particles were observed on the surface of the microgels. As the pyrrole content increases from 0 to 70 wt%, the microgel's shape gradually changes from spheres to raspberry-like particles, with their size decreasing from  $185 \pm 6$  to  $129 \pm 9$  nm. This phenomenon is a result of the cross-linking effect and hydrophobicity of PPy on the microgels. The hydrophilic polymeric chains of microgels significantly improve the stability of PPy in water, and no aggregation or precipitation was found after 1 month of storage (Figure S3, Supporting Information). The conductive hydrogels were synthesized by the free radical polymerization of acrylamide, lauryl methacrylate (LMA), and PM-50 initiated using ammonium persulfate and tetramethyl ethylenediamine (Figure 2a). The hydrogels were designated as HPM-*Y*, where *Y* is the mass percentage of PM-50 in the hydrogels (Table S2, Supporting Information). Pure PPy shows poor compatibility with hydrogel networks as a result of the highly hydrophobic feature, which leads to the aggregation of PPy particles and

deteriorates the mechanical properties of hydrogels. Herein the microgels were used as carriers for PPy to incorporate more PPy components without any compromise on the mechanical properties of the hydrogels. The morphology of the hydrogels was characterized by a cryo-scanning electron microscope, which shows the uniform distribution of PM-50 within the hydrogel matrix (Figure 2e).

The mechanical properties of the HPM-*Y* were investigated through tensile and compression measurements. As shown in **Figure 3a**, the elongation at break increases with the increase in PM-50 contents. The elastic moduli of all HPM-*Y* samples are in the range of 17–32 kPa (Table S3, Supporting Information), which matches the elastic modulus of biological tissues (10–100 kPa). HPM-1 shows superior mechanical performance with a maximum tensile strength of 196 kPa, an elastic modulus of 29 kPa, and an elongation at break of 1950%. Then, a suit of tensile loading–unloading tests was performed on HPM-1 (Figure S4, Supporting Information). The hysteresis loops of HPM-1 nearly overlap for the five tensile test cycles, indicating that the HPM-1 retains the same interior network structure during the tensile cycles. To further understand the energy dissipation mechanism at the molecular level, the role of sodium dodecyl sulfate (SDS) also has been investigated (Figures S5 and S6, Supporting Information). An interesting phenomenon was observed about the SDS influence on the mechanical performance of the hydrogels. When the SDS concentration increases from 0% to 1%, the tensile strength increases from 5.6 to 196 kPa (Table S4, Supporting Information). If the SDS concentration further increases beyond 1%, the tensile strength exhibits a decreasing trend with the SDS concentration. It has been reported that a gradual softening of hydrogels occurs in the presence of surfactant.<sup>[39]</sup> In this work, a bridge structure was formed between microgels and hydrogel networks via SDS (Figure 2a). The SDS connector bonds to microgels by the electrostatic interaction between sulfate groups and PPy while the dodecyl groups of SDS can form a hydrophobic association with the LMA groups in the polymer networks. The SDS connector is capable of dissipating applied energy from polymer networks



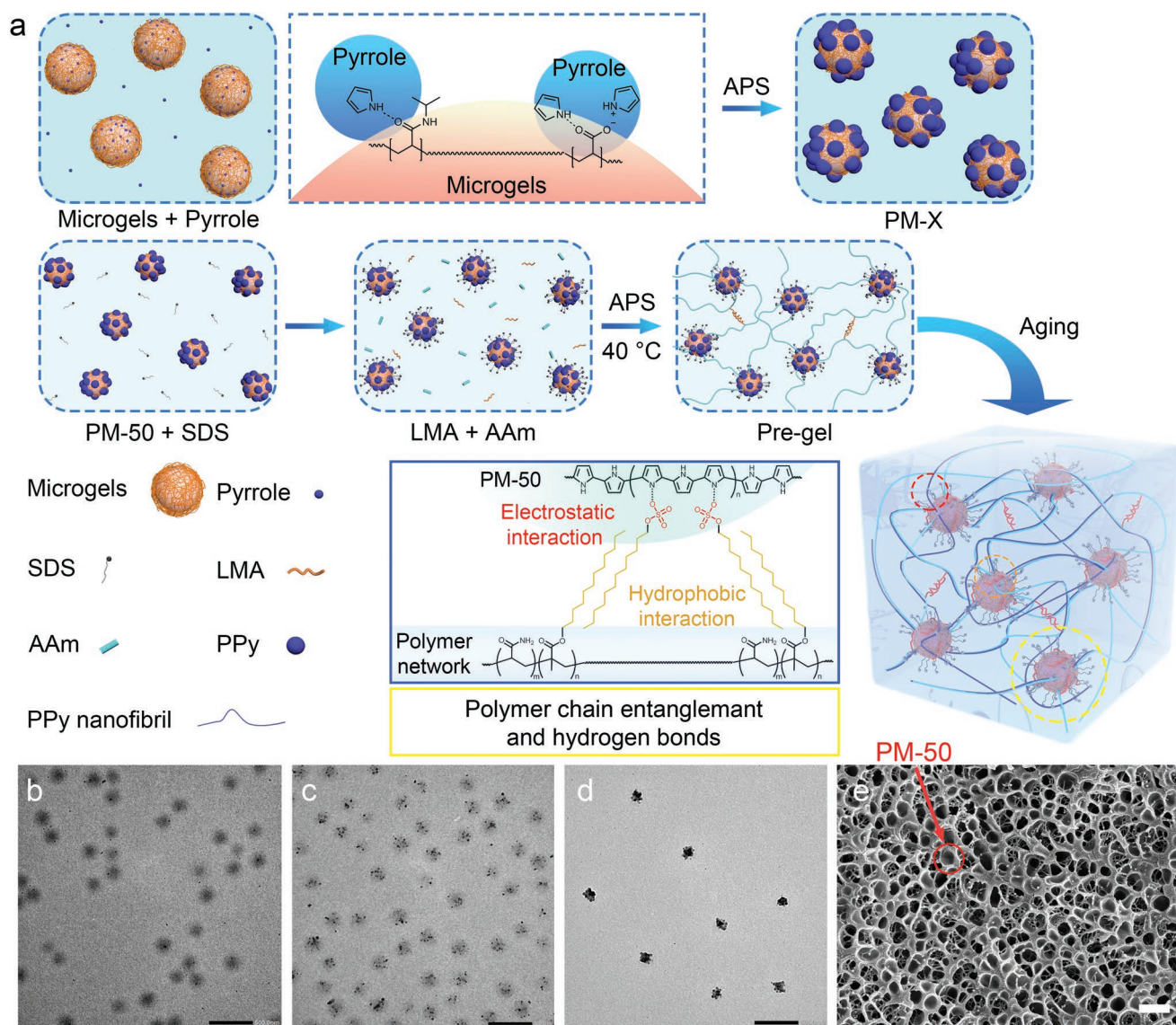


**Figure 2.** a) The synthesis of PM-X and HPM-Y. b–d) TEM images of PM-0 (b), PM-10 (c), and PM-50 (d) (scale bar: 500 nm). e) The cryo-SEM image of HPM-1 (scale bar: 500 nm).

to microgels. In addition, the fatigue resistance of HPM-1 was assessed by performing 200 consecutive tensile testing cycles at the strain of 200% and 500% (Figure S7, Supporting Information). No performance loss was found during the 200 tensile cycles, which demonstrates excellent fatigue resistance. The compression measurement was also conducted (Figure 3b). All the HPM-Y samples show almost the same tensile-strain variation in the low strain range (<50%), while the microgels show a significant influence on the stress–strain relation in the high strain range (50–90%). The microgels demonstrate the same influence trend on the stress–strain relation during the tensile and compression measurements. Subsequently, the HPM-1 was subjected to a cyclic compression test with various strains (Figure S8, Supporting Information). The compression stress and dissipation energy show exponential growth with the strain, which is a typical elastic characteristic. The compression stress and dissipated energy of HPM-1 at 90% strain were up to

1.15 MPa and  $0.071 \text{ MJ m}^{-3}$ , respectively. 200 continuous compression tests at the strains of 20% and 50% were carried out to investigate the fatigue resistance for compression (Figure 3c). HPM-1 exhibits a constant compressive strength during the 200 loading–unloading cycles. These aforementioned results manifest an outstanding anti-fatigue performance of HPM-1 for mechanical deformation. Fatigue is a major problem for sensing interfaces which can affect the formation of compliant sensing interfaces with dynamic organs. The excellent fatigue resistance enables HPM-1 to form compliant sensing interfaces with dynamic structures in the body and maintain structural integrity under cyclic deformation, which reduces signal loss and avoids the potential toxicity caused by structural degradation. This lends HPM-1 as a suitable sensing material. Figure 3d shows a comparison of mechanical performance between HPM-1 and other hydrogels used as wearable or implantable sensors reported in the literature. Compared with hydrogels

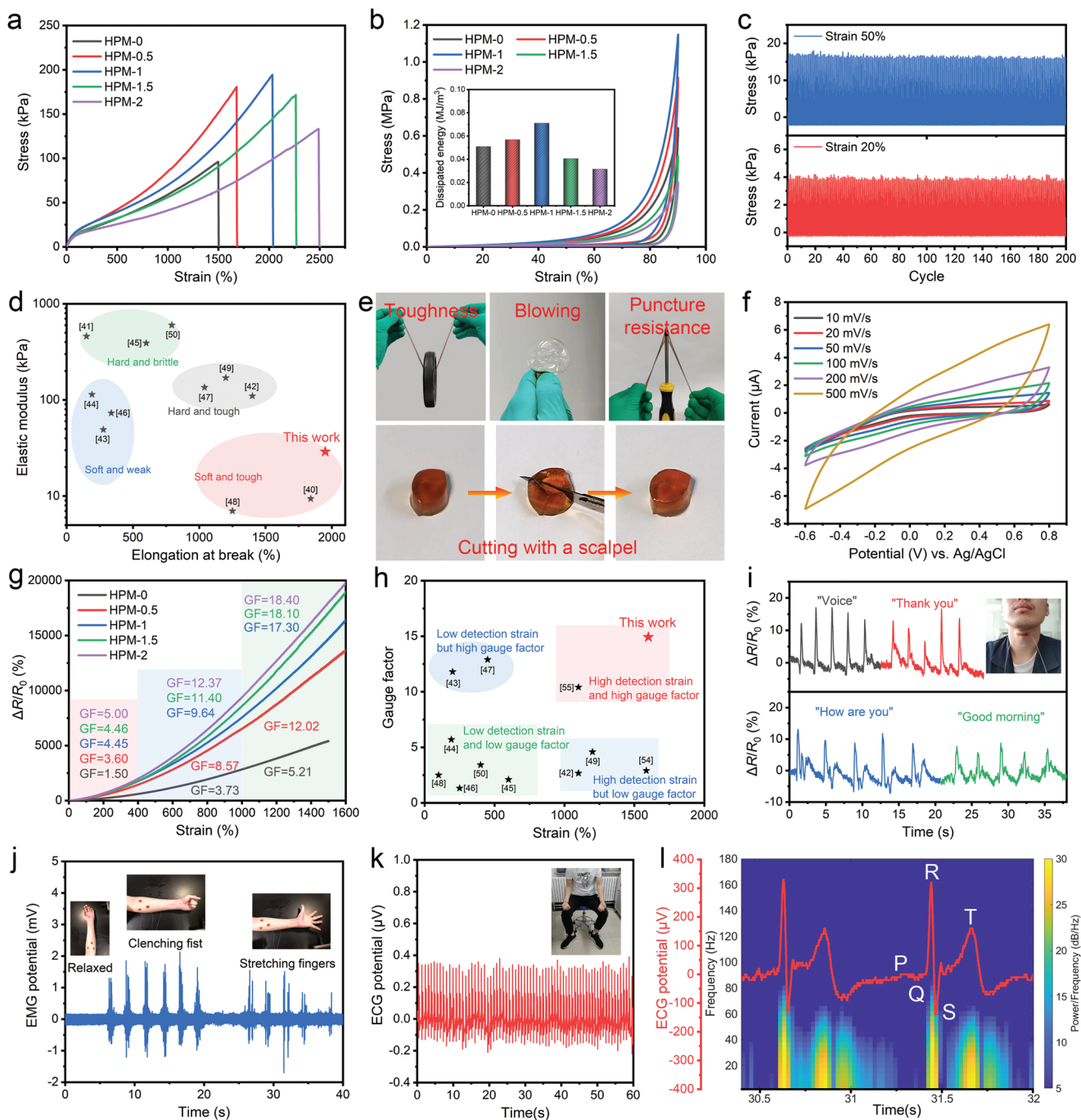


**Figure 3.** a) Tensile stress–strain curves of HPM-Y. b) Compressive stress–strain curves and calculated dissipated energy of HPM-Y. c) 200 consecutive compression cycles of HPM-1 under 20% and 50% strains. d) Comparison of HPM-1 with other hydrogel sensors in terms of elastic modulus and elongation at break. e) Mechanical performance demonstration of HPM-1 for lifting a weight plate, stabbing with a screwdriver, cutting with a scalpel, and blowing with a N<sub>2</sub> flow. f) The CV curves of an HPM-1 electrode at different scanning rates (10–500 mV s<sup>-1</sup>). g) Resistance changes as a function of strain for HPM-Ys. h) Comparison of HPM-1 sensor with other reported hydrogel strain sensors in terms of maximal strain and GF. i) The real-time resistance signals when a volunteer was speaking. j) The EMG signals of a volunteer. k) ECG testing on the skin using HPM-1 electrode. l) Spectrogram of the ECG pulse recorded using HPM-1 electrode.

modified by traditional rigid nanofillers (such as carbon nanotubes, SiO<sub>2</sub>, and graphene), HPM-1 has a lower elastic modulus and higher stretchability.<sup>[40–50]</sup> This phenomenon is a result of the deformation behavior of microgels when applying external stress. Once the external stress was withdrawn, the microgels

are capable of recovering to their original status.<sup>[51]</sup> The robust mechanical performance of HPM-1 also has been qualitatively demonstrated (Figure 3e). A 0.75 kg barbell plate can be lifted using an HPM-1 sheet of 3.0 cm × 1.0 cm × 0.4 cm. The HPM-1 sheet can be deformed and inflated into a balloon upon



exposure to a  $N_2$  flow, as evidence of its excellent stretchability. Furthermore, the HPM-1 sheet can withstand vigorous puncturing by a screwdriver and squeezing by a sharp scalpel blade with no observable damage, which attests to its inherent excellent puncture and scratch resistance.

The mechanical performance of the hydrogels was further characterized using rheological tests to study viscoelastic, anti-fatigue, and self-recovery performances. Figures S9 and S10, Supporting Information, show the storage modulus ( $G'$ ) and loss modulus ( $G''$ ) of HPM-Y as a function of frequency. The  $G'$  and  $G''$  were determined to be in the range of 1.1–11.4 and 0.5–1.3 kPa, respectively. The  $G'$  was always larger than  $G''$  over the entire frequency range (0.1–100  $\text{rad s}^{-1}$ ) and both of them were insensitive to frequency changes. The phenomenon suggests that the elastic response is a predominant feature of HPM-Y. The HPM-1 was subjected to a strain amplitude sweep test in the strain of 0.1–1000% to investigate the limit of the linear viscoelastic region (Figure S11, Supporting Information). The  $G'$  and  $G''$  were constant in the shear strain range of 0.1–30%, indicating the HPM-1 in a gel (solid) state. The  $G'$  and  $G''$  curves intersected at the strain of 303% for HPM-0 and 382% for HPM-1, which is the critical point between the gel and sol states. These results demonstrate the important role of microgels in enhancing the stretchability and flexibility of HPM-Y. In addition, cyclic shear strain testing was applied to investigate the self-recovery performance of HPM-1. As shown in Figure S12, Supporting Information, a small strain of 0.5% for 180 s and a large strain of 400% for 60 s were alternatively applied to the HPM-1. HPM-1 was in a sol and gel state at large shear strain and small shear strain, respectively. After switching from 400% strain to 0.5% strain, the modulus recovered to its original value within 20 s attesting to its excellent self-recovery performance.

## 2.2. Recording Physiological Signals

The electrochemical properties of the HPM-1 were investigated by cyclic voltammetry (CV) and electrochemical impedance spectroscopy. No redox peak was observed in the CV curves at various scanning speeds (10–500  $\text{mV s}^{-1}$ ) indicating that no electrochemical reaction occurs during the test (Figure 3f). The charge storage capacity of 6.92  $\mu\text{C}$  was obtained from the CV results. Then HPM-1 was subjected to 1000 CV cycles, and less than 5% change in charge storage capacity was found indicating excellent electrochemical stability (Figure S13, Supporting Information). Furthermore, it shows the same impedance value ( $\approx 23.5 \text{ k}\Omega$ ) at the frequency of 1 kHz after 1000 CV cycles as evidence of high electrochemical stability (Figure S14, Supporting Information). Conductivity is an incredibly important parameter that determines materials' applicability for electrochemical sensing applications. The conductivity of HPM-Y was determined by a four-probe tester to be 0.34–1.40  $\text{S m}^{-1}$  dependent on the PM-50 content (Figure S15, Supporting Information). For comparison, a hydrogel (H-PPy) was prepared by the polymerization of hydrogel precursor in the presence of PPy nanoparticles (the same content of PPy with HPM-1), which exhibits a conductivity of 0.52  $\text{S m}^{-1}$ , much lower than that of HPM-1 (1.17  $\text{S m}^{-1}$ ). This result is attributed to the inevitable aggregation of PPy particles in the hydrogels. Figure S16, Supporting Information, shows the comparison of HPM-1 with other transparent hydrogels for bioelectronics in the literature on

conductivity and stretchability.<sup>[47–50,52–55]</sup> The HPM-1 exhibits superior performances in terms of conductivity and stretchability. To qualitatively demonstrate the conductive property, an HPM-1 sheet and column were used as conductors to link a power source and a LED. As a 3 V voltage was applied to the circuit, the LED was lit up and the brightness of the LED was affected by hydrogel deformation such as stretching or compression (Figure S17 and Video S1, Supporting Information). Figure 3g shows the resistance changes as a function of the HPM-Y strain. The curve slope, known as the gauge factor (GF), is used to represent the sensitivity of strain sensors.<sup>[56]</sup> The GF values of the HPM-Y samples increase with increase in PM-50 content. For example, the HPM-0.5 shows GF values of 3.60, 8.57, and 12.02 while HPM-2 shows GF values of 5.00, 12.37, and 18.40 in the strain ranges of 0–400%, 400–1000%, and 1000–1600%, respectively. Repeatability was evaluated in the range of 0.5–1500% by conducting the test five times at each strain. The same resistance change–strain curves were observed at each strain (Figure S18, Supporting Information). A similar result was obtained for the compression test in the strain range of 10–60% (Figure S19, Supporting Information). These results indicate excellent repeatability of HPM-1 during the strain–resistance change tests. The  $\Delta R/R_0$  is independent of tensile or compressive rates (Figures S20 and S21, Supporting Information), suggesting no electrical hysteresis during the deformation process. Durability and fatigue resistance were investigated by subjecting HPM-1 to 100 continuous tensile cycles at the strain of 200% and 200 continuous compression cycles at the strains of 50% (Figures S22 and S23, Supporting Information). No performance loss was observed for HPM-1 sensors during these continuous cycles, which indicates excellent fatigue resistance and stability. The comparison of the HPM-1 sensor with other reported hydrogel strain sensors in terms of maximal strain and GF has been shown in Figure 3h.<sup>[42–50,54,55]</sup> The HPM-1 sensor exhibits a larger GF and broader strain range than these strain sensors. The excellent mechanical performance and conductivity enable the HPM-1 to be used as a wearable strain sensor for recording physiological signals. As shown in Figure S24, Supporting Information, when HPM-1 sensor was installed on the heels of two volunteers (75 and 45 kg), a series of characteristic peaks were obtained during the subjects' movements (e.g., walking, running, and jumping). The shape and intensity of characteristic peaks are affected by the walking posture and body weight of volunteers, respectively. Furthermore, the HPM-1 sensor shows the capability of monitoring more sophisticated motions such as vocal cord vibrations and subtle epidermal deformations during talking. Figure 3i shows the characteristic peaks acquired by the HPM-1 sensor when speaking different words such as “voice,” “thank you,” “good morning,” and “how are you.” The pronunciation generates characteristic peaks verified by repeatedly testing five times for each word. These results indicate that the HPM-1 sensor has the capability of voice recognition, which can find applications in vocal cord recovery and telovox applications. EMG is an important diagnostic tool to assess the health status of muscles and the nerve cells such as muscle and nerve disorders. The HPM-1 electrode pad was further utilized to obtain EMG by recording the compound action potentials generated by the activation of muscle. As shown in Figure 3j, three HPM-1 electrode pads were attached to the flexor muscle (left arm) of a 23 year old female. When the volunteer conducted some actions such as clenching and releasing a fist, two groups of characteristic bursts were observed in the EMG. The signal–noise ratio

of EMG acquired by the HPM-1 electrode is 19.6 dB calculated by the ratio of signal amplitude to baseline noise. The result demonstrates that the HPM-1 electrode is capable of acquiring high-quality EMG signals. ECG is widely used to diagnose and monitor heart conditions including arrhythmias, coronary heart disease, and heart attacks. The HPM-1 electrode was used to measure ECG by attaching it to the left/right wrists and left ankle of a healthy volunteer (Figure 3k). The waveforms show typical ECG waveforms with P-wave (atrial depolarization), QRS complex (ventricular depolarization), and T-wave (ventricular repolarization). In addition, the spectrogram of the ECG pulse is obtained by Fourier

transformation (Figure 3l). PQRST peak frequency can be clearly identified, which is useful for the auxiliary diagnosis of various cardiac abnormalities.<sup>[57]</sup>

### 2.3. Recording Brain Neural Signals

Biocompatibility is a requisite feature for the HPM-1 electrode applicability as implantable sensors for recording brain neural signals. We first evaluated the in vitro cytotoxicity of HPM-1 by measuring the viability of rat Schwann cells (RSC-96) (Figure 4a

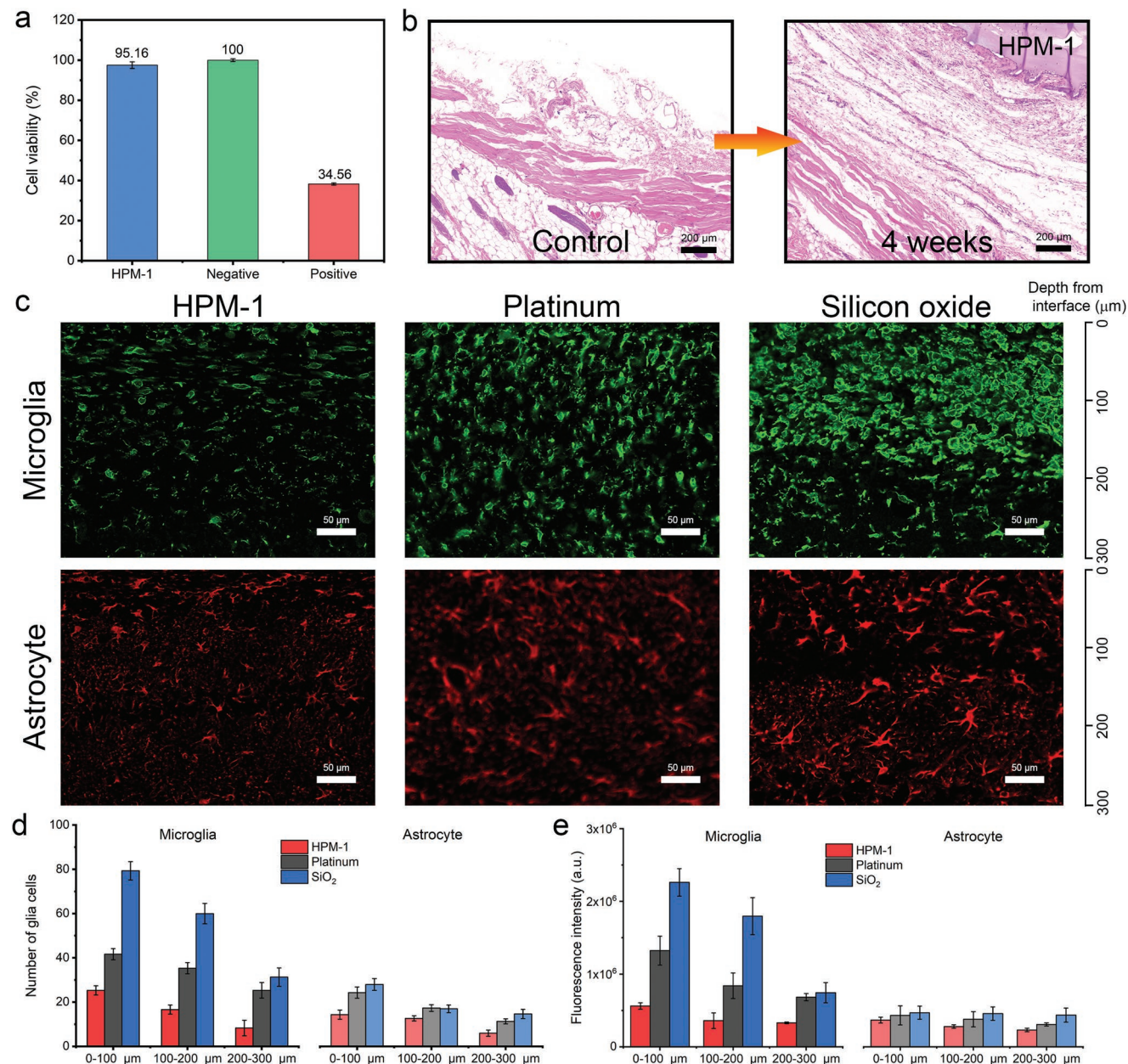


**Figure 4.** a) The viability of RSC96 cells in 1 mg mL<sup>-1</sup> leaching solution for 24 h. b) H&E histological results of the control and HPM-1 samples after 4 weeks of implantation, respectively. c) Confocal microscopy images of the brain slices: microglia cells (green) and astrocyte cells (red). d) The statistical numbers of microglia and astrocyte cells within the square area of 300 × 300 μm in the depth range of 0–100, 100–200, and 200–300 μm from these electrodes. e) The mean fluorescence intensities of the cell counting areas in these confocal images.

and Figure S25, Supporting Information). The cell morphology and proliferation were studied after 24 h incubation in 1 mg mL<sup>-1</sup> leaching solutions. It was evident that only viable cells (green stained) and almost no dead cells (red stained) were observed in the live and dead assay. The cell viability is larger than 95% after 24 h incubation in all experiments, demonstrating negligible cytotoxicity of HPM-1 to RSC96 cells. An HPM-1 sheet was implanted into the subcutaneous region of rats for 4 weeks to investigate in vivo cytotoxicity. Histology analysis using hematoxylin and eosin staining reveals no inflammatory response during the 4 weeks of implantation (Figure 4b). It was further evident that HPM-1 maintained a close contact boundary with the tissue during the implantation period indicative of matching biomechanical performance and excellent biocompatibility. The HPM-1 was then implanted into the rat's hippocampus CA1 region to study immune response. Platinum and SiO<sub>2</sub> (optical fiber) are the commonly used materials for recording brain neural signals and optogenetics, respectively. As such, for comparison, the immune response of platinum and SiO<sub>2</sub> was also investigated. After a week, the interfacial parts between hippocampus tissues and electrodes were sliced and immunohistochemically treated for immune response investigation. As shown in Figure 4c, much fewer glial cells around the HPM-1 are observed compared with those near platinum and SiO<sub>2</sub>. The numbers of glial cells in the square areas of 300 × 300 μm were quantified in the depth range of 0–100, 100–200, and 200–300 μm relative to the interfaces in Figure 4d. The number of glial cells significantly increases in the brain tissue closer to these implants, which is attributed to the unmatched mechanical performances of the implants. Glial cells gradually migrate to the implants and form a glial sheath to protect the brain tissue. The glial sheath squeezes neurons away from the implant's surface. Meanwhile, the fluorescence analysis of the slices was also conducted (Figure 4e). The fluorescence intensity of the slice near the HPM-1 electrode was significantly lower than those near platinum and SiO<sub>2</sub> electrodes, which further indicates the excellent biocompatibility of the HPM-1.

The excellent biocompatibility and electrical conductivity make the HPM-1 electrode a suitable neural probe for recording LFPs in rat brains. The LFPs show the aggregate activity of small populations of neurons, which reflect the highly dynamic flow of information in neural networks.<sup>[58]</sup> It can be used to evaluate the comprehensive electrophysiological activity of local brain tissues in the range from a few hundred micrometers to a few millimeters away from electrodes. To obtain stable LFP signals, a device containing HPM-1 and reference electrodes was fabricated, which can be fastened on the skull of rats for long-term recording (Figure 5a–c). The HPM-1 electrode was prepared by injecting the HPM-1 into a flexible Teflon microtube. The flexible and insulating Teflon microtube shields electric signals from other parts of neural networks to ensure the signals only recorded through the electrode tips by the HPM-1. The HPM-1 electrode was implanted in the hippocampus CA1 regions of anesthetized rats to investigate the capability of recording brain neural signals. The LFPs of the anesthetized rats are typically dominated by delta rhythm (0–2 Hz). When the tails of rats were clamped by a clipper, the LFPs were dominated by theta rhythm (2–7 Hz) (Figure 5d). This phenomenon results from the enhanced activation of interneurons and suppressed

excitability of pyramidal cells caused by somatosensory stimulation. Similar results of SEP experiments also have been reported in the literature.<sup>[59]</sup> Furthermore, when HPM-1 electrode was implanted in the hippocampus CA1 regions of free-moving rats, the LFP signals show obvious differences in the awake and sleeping states of the rats (Figure 5e and Video S2, Supporting Information). The LFP signals in the sleeping state show a much larger amplitude than those in the awake state. The time-domain signals were transformed into spectrograms by a short-time Fourier transform to acquire frequency information (Figure 5e). The spectrograms in the sleeping state show a frequency range of 3–12 Hz with larger power as a result of theta oscillations. The theta oscillation waves result from the synchronized activity of a large number of neurons produced by mammals during sleeping. These transient increases in theta frequency and power are associated with an increased firing rate and coordination throughout the hippocampus in the sleeping state.<sup>[60]</sup> Similar LFP signals of rats have been also reported in the literature.<sup>[61–63]</sup> For comparison, traditional platinum and HPM-0 electrodes were used to record the LFPs, respectively (Figure 5e). The HPM-0 electrode without PPY was infused with artificial cerebrospinal fluid (ACSF) to achieve good ion conductivity. The ACSF is a biocompatible electrolyte commonly employed in obtaining extracellular electrophysiological signals.<sup>[63]</sup> The LFP signals with larger amplitude were recorded by the platinum electrode, which is attributed to the lower impedance of the platinum electrode. While, the LFPs obtained by the HPM-0 electrode show a much lower intensity than that recorded by the HPM-1 electrode. The lower signal intensity is a result of lower conductivity caused by ion diffusion in the brain tissue. Apparently, the relatively strong and stable LFP signals can be obtained by the HPM-1 electrode. For the investigation of the long-term applications, the HPM-1, platinum, and HPM-0 electrodes were implanted into the hippocampus regions of rats to continuously record LFP signals for 8 weeks. Figure 5f shows the changes in these LFP signals in a sleeping state with time. While the LFP signals obtained by platinum electrodes show a higher intensity for the first 2 weeks, their intensity reduced to much lower levels since the 3rd week compared to the HPM-1 electrode. The HPM-0 electrode produces LFP signals with the lowest intensity among the three electrodes. The HPM-1 electrode can obtain relatively stable LFP signals during the 8 weeks of implantation, as evidence of an excellent implantable probe for long-term recording of brain neural signals. To investigate the discrepancy in signal attenuation with time, the hippocampus tissues on the interface with electrodes were sliced for immunological study. Massive glial cells were observed in the hippocampus tissues around the platinum electrode (Figure S26, Supporting Information). The glial cells block the electron transmission pathway from the hippocampus tissue to the electrode, which resulted in signal attenuation with time.<sup>[64,65]</sup>

#### 2.4. Optogenetic Neuromodulation

Understanding the information generation and transfer within the human brain is a great challenge. To address this challenge there is a need to develop tools with the capacity for probing the



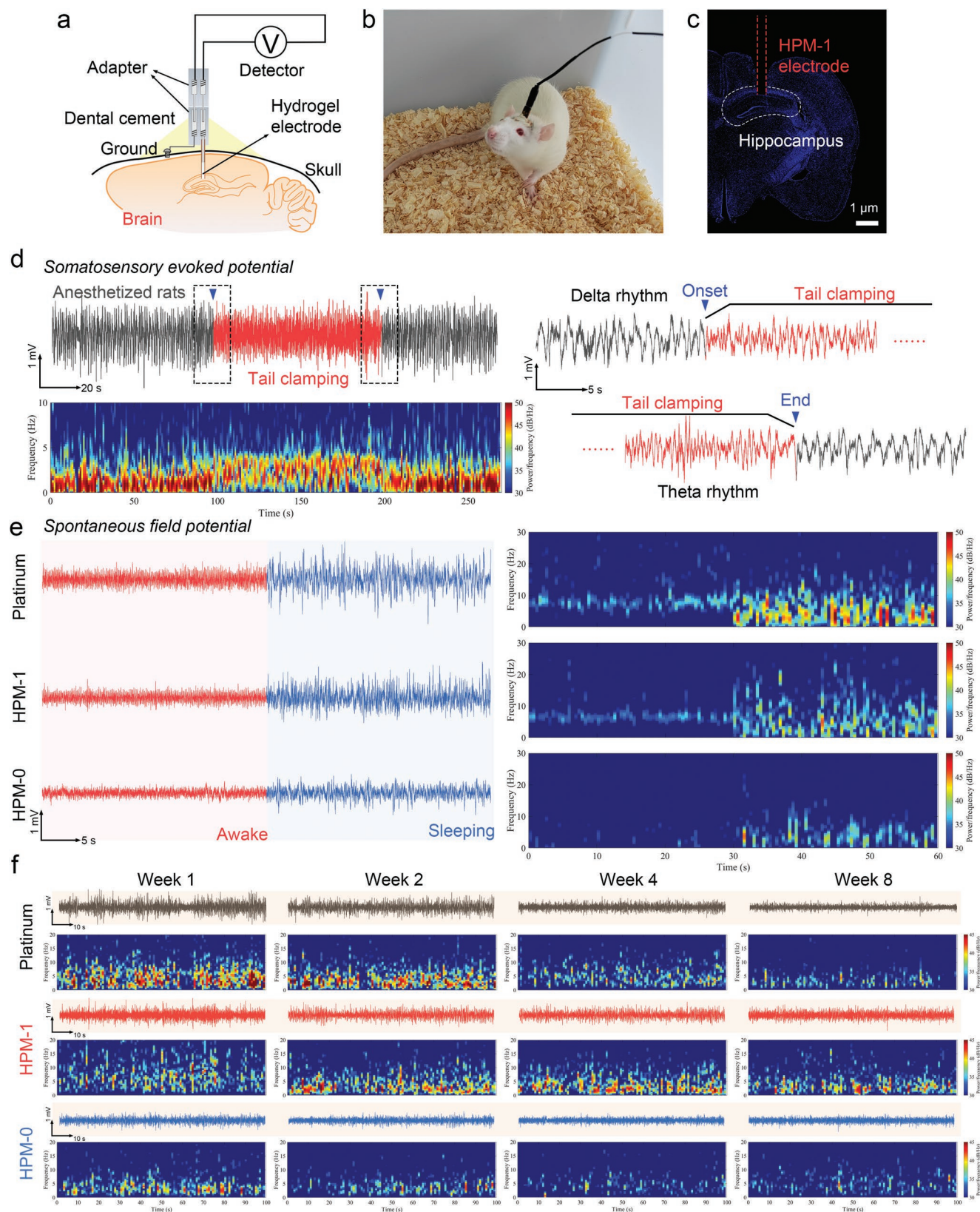


**Figure 5.** a) Schematic diagram of the detection device for free-moving rats. b) Photograph of a rat implanted with an HPM-1 electrode. c) A microscopy image of an HPM-1 electrode implanted in a rat brain (DAPI was used as a nuclear fluorescent stain). d) LFPs of rat's hippocampus CA1 region recorded by an HPM-1 electrode. e) LFPs recorded by platinum, HPM-1, and HPM-0 electrodes. f) LFPs recorded in the sleeping state by platinum, HPM-1, and HPM-0 electrodes for 8 weeks of detection.

dynamics of nervous systems while simultaneously recording neural signal variations in relation to behaviors. It has been reported that pulsed-light flashes can cause transmembrane ion flow and result in neuron firing in channelrhodopsins (ChR)-functionalized brain neurons.<sup>[66]</sup> Here the light-mediated neural circuitry modulation was conducted using the HPM-1 electrode. Besides electron conductivity, the transparency of electrodes is another important performance for optogenetic modulation. The transparency of the HPM-1 was characterized, which is much higher than that of H-PPy (the same PPy content) (Figure 6a). The higher transparency is attributed to the

small size of microgels carriers that allows the optical wave to bypass these nanoparticles and minimize the particle–light wave interaction. The refractive index of HPM-1 was measured by a refractometer to be 1.40, which is similar to the refractive indices of the tissue (1.33–1.51).<sup>[67]</sup> The optical power transmission efficiency was determined at 465 nm to be  $83.2 \pm 0.5\%$ , yielding the optical loss index of  $0.2 \text{ dB mm}^{-1}$ . The special structure renders the HPM-1 electrode both high conductivity and high transparency (Figure S16, Supporting Information). This synergy overcomes the tradeoff between conductivity and high transparency suffered by electron-conductive hydrogels.

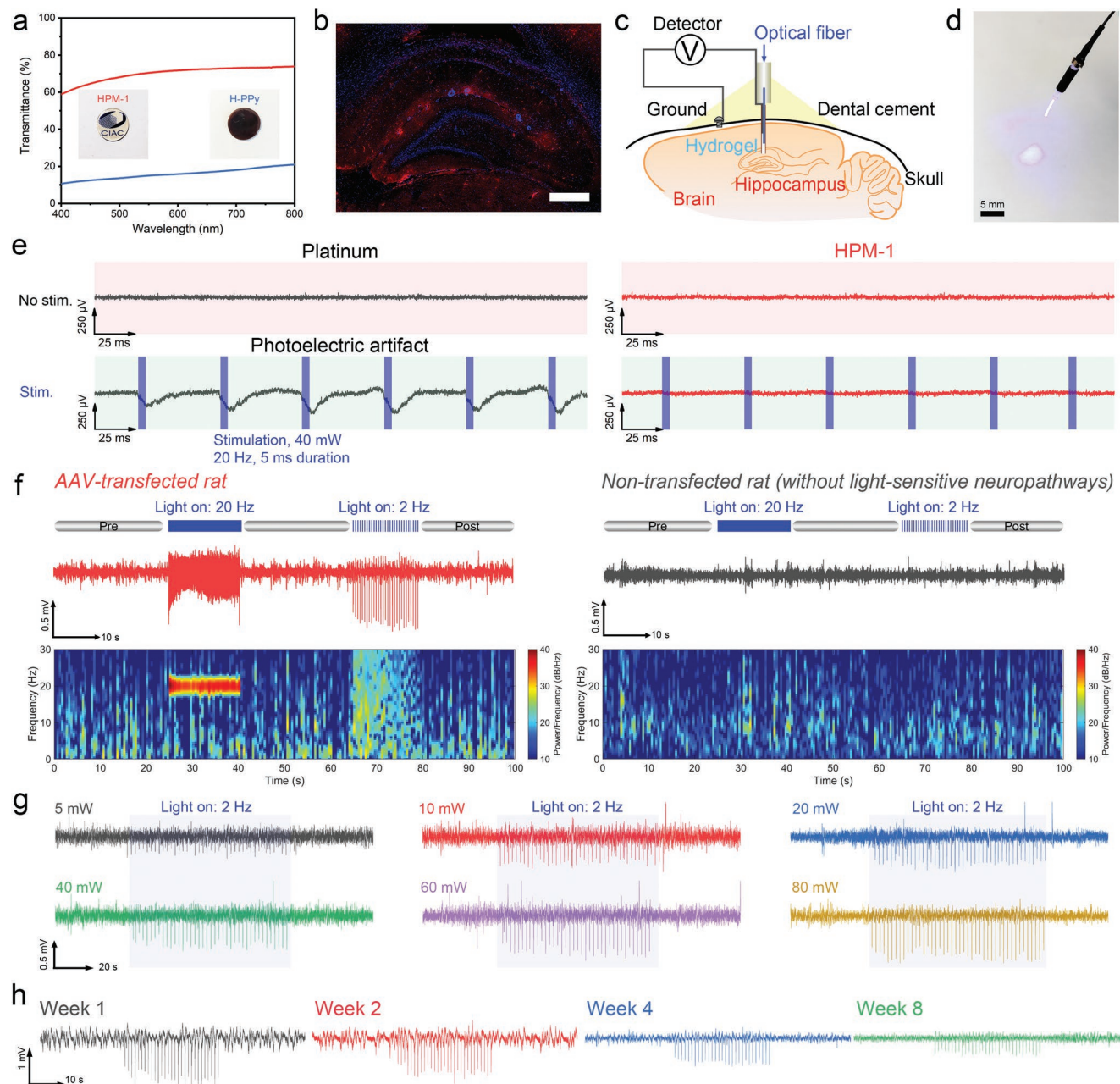


**Figure 6.** a) The UV–vis transmittance curves and photographs of the HPM-1 and H-PPy with a thickness of 1 mm. b) Expression of AAV (red) in the hippocampus after 4 weeks transfection (scale bar: 500  $\mu\text{m}$ ). c) Schematic diagram of the device for optogenetic modulation and recording LFPs. d) Photograph of an HPM-1 optrode. e) Photoelectric artifact experiments of platinum optrode (left) and HPM-1 optrode (right). f) Optogenetically evoked LFPs and the corresponding spectrogram. g) The optogenetically evoked LFPs tuned by different light power. h) The optogenetically evoked LFPs recorded by HPM-1 for 8 weeks.



Before the optogenetic neuromodulation, the neurons were transfected by adeno-associated virus (AAV)-CaMKII $\alpha$ -ChR2-mCherry to create light-sensitive neuropathways. The light-responsive ChR was observed in the nervous system after 4 weeks of transfection (Figure 6b). HPM-1 optrode was prepared by embedding an optical microfiber embedded in an HPM-1 electrode to conduct optogenetic activation (Figure 6c). It can be seen that blue light pulses can penetrate the HPM-1 in Figure 6d. Photoelectric artifact is a significant challenge of metal-based neural electrodes, which generates electrical noises and contaminates electrophysiological data. As such the photoelectric artifacts of the platinum and HPM-1 optrodes are investigated by applying a blue laser (472 nm, 20 Hz, 5 ms duration) before the optogenetic neuromodulation (Figure 6e). The platinum optrode shows a photoelectric artifact of  $\approx 100 \mu\text{V}$ , while almost no photoelectric artifact is observed for the HPM-1 electrode. These results indicate the significant advantage of the HPM-1 over platinum in optogenetics. Figure 6f shows the LFP signals recorded by the HPM-1 optrode when activated by the blue light pulses (2 and 20 Hz, 5 ms duration). The blue light pulses can generate clear LFP signals in AAV-transfected rats and the frequencies of the LFP signals are associated with those of the light pulses. Furthermore, the

intensities of LFP signals can be tuned by controlling the power of light pulses (Figure 6g). For comparison, an HPM-1 optrode was also implanted into wild-type rats without AAV transfection, and no LFP signal was obtained when activated by the blue light pulses. These results suggest that the HPM-1 optrode also does not produce photoelectric artifacts in the brains of rats.<sup>[68]</sup> As such the fabricated HPM-1 device can realize the synergistic function of in vivo optogenetic neuromodulation and neural signal monitoring. Then the durability of the HPM-1 device was investigated by conducting optogenetic neuromodulation and simultaneously recording the LFP signals for 8 weeks. The LFP signals show negligible loss during the 8 weeks test, attesting to the excellent capability of HPM-1 for optogenetic neuromodulation during long-term applications (Figure 6h). The neuronal spike is a main inter-neuronal communication way for brain neurons, which plays an important role in cognition function. The HPM-1 electrode was used to detect the neuronal spike from a single neuron in the hippocampus CA1 regions of rats. The HPM-1 electrode was manufactured with a diameter of  $5 \mu\text{m}$  to match the neuron size ( $20\text{--}50 \mu\text{m}$ ) and an optical fiber was integrated to conduct light stimulation on the neurons (Figure 7a). As the HPM-1 electrode approaches a neuron, neuronal spike

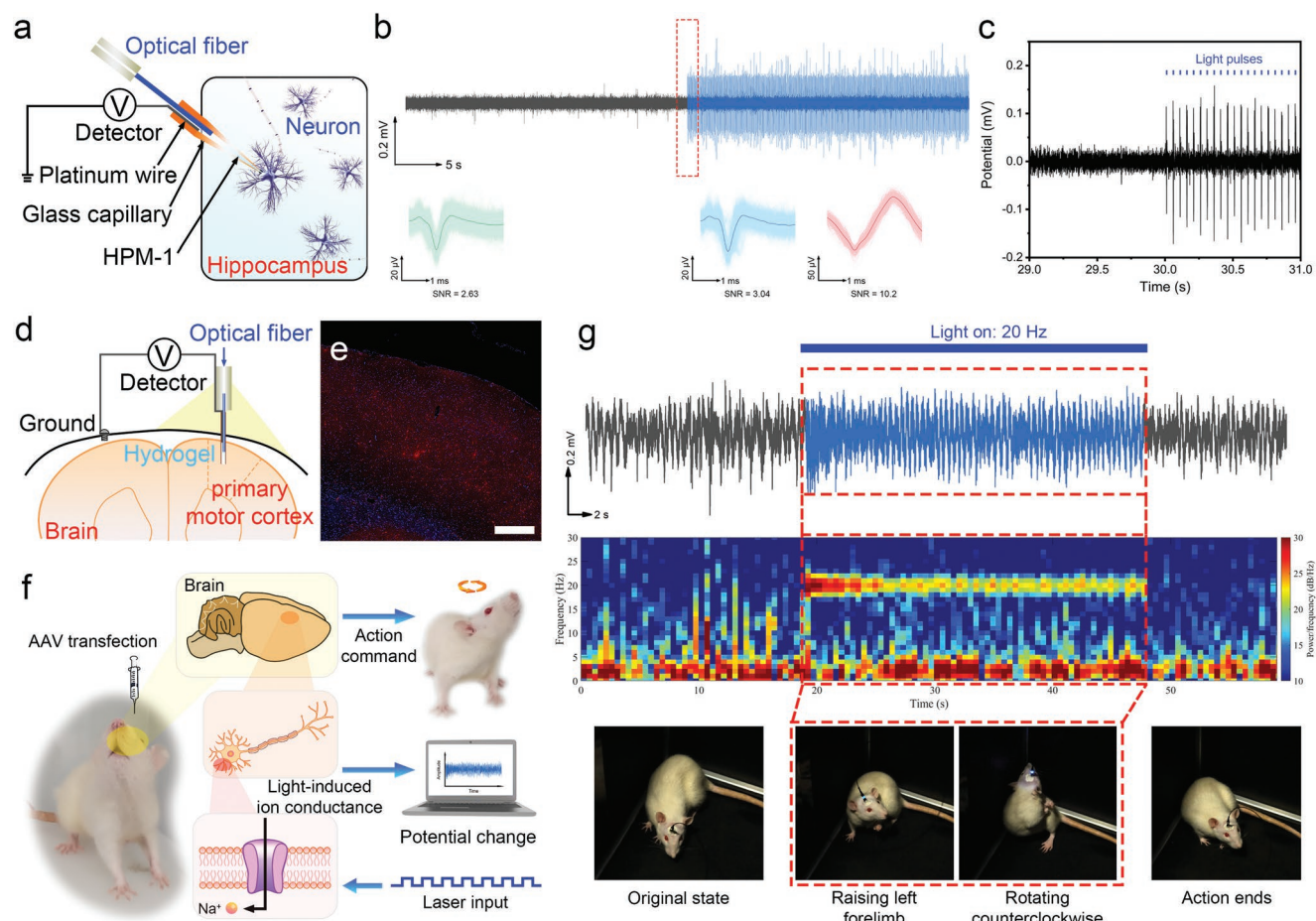


**Figure 7.** a) The device for recording neuronal spikes in vivo. b) The spikes and their overlapped waveforms of a rat recorded by HPM-1 in vivo. c) The neural spikes of a single neuron in response to the blue light pulses. d) Schematic diagram of the device for optogenetic modulation and recording the neural signals in the right primary motor cortex region of free-moving rats. e) Expression of AAV (red) in the right primary motor cortex region after 4 weeks transfection (scale bar:  $500 \mu\text{m}$ ). f) Schematic diagram of optogenetic modulation of animal behavior and electrophysiological signal acquisition. g) The correlation between brain neural signals and resulting behaviors modulated by blue light pulses (20 Hz).



signals were obtained, as shown in Figure 7b. The neuronal spike signals were analyzed by an algorithm method reported by Toosi et al.<sup>[69]</sup> 1002 spikes recorded in 30 s were overlapped to generate a statistical waveform of neural spikes in Figure 7b. We further used the signal-to-noise ratio ( $SNR_{\text{spike}}$ ) to evaluate the capability of sensing neural spikes. The  $SNR_{\text{spike}}$  was determined to be 2.63. The neural spikes of a single neuron in response to the blue light pulses have also been investigated in Figure 7b,c. Each flash of the laser pulse leads to a large electrophysiological signal generated by the activated neuron. The statistical waveform of neural spikes shows two types of neural spikes that were assigned to normal neuron firing and optogenetic neuromodulation, respectively (Figure 7b). It is very intriguing to further investigate the relationship between rat behavior and neural signal triggered by blue light pulses. Here the HPM-1 electrode was implanted into the right primary motor cortex region of rats transfected by AAV for optogenetic neuromodulation and simultaneous behavior investigation (Figure 7d–f). Blue pulses (20 Hz, 5 ms duration, 20 mW) were applied to the primary motor cortex region. Although the primary motor cortex region has well-known responsibility for controlling limb behavior, to the best of our knowledge, the correlation between brain neural signals in the primary motor cortex region and corresponding limb behavior has yet to be reported during optogenetic neuromodulation. The clear and regular neural signals were detected by the HPM-1 device, and the frequency (20 Hz) of these signals matches well with that of blue pulses (Figure 7g). Once the blue light pulses were applied, the rat immediately raised its left forepaw and after a few seconds, the entire body started to twist in a counterclockwise direction (Figure 7g and Video S3, Supporting Information). When the light stimulation was terminated, the neural signals disappeared and the rats immediately stopped the twisting behavior and returned to their original calm status.

### 3. Conclusion

A strategy has been proposed to address the tradeoff between conductivity and transparency suffered by most electron conductive hydrogels, which is a barrier for implantable sensor electrodes used for neurological brain studies. It has been demonstrated that by confining the conductive component to the microgels' surface, the particles–light wave interaction is minimized which increases the transparency of the electrode materials while maintaining excellent electron conductivity. Through a special supramolecular structure with microgels as large cross-linking centers in hydrogel networks, another great tradeoff between conductivity and mismatch modulus between the biological tissues and implantable electrodes has also been resolved. The hydrogels exhibit a matched modulus with brain neural tissue, excellent stretchability, and remarkable fatigue resistance. These unique biomimetic chemo-mechanical performances reduce electrode micromotion, minimize adverse biological responses, and improve signal transmission through biohybrid interfaces, which render the hydrogels highly feasible for implantable sensory applications. The HPM-1 electrode was successfully utilized to in situ record LFPs by implanting it into the hippocampus CA1 regions of rats with

stable signals and negligible signal attenuation for 8 weeks. The HPM-1 electrode shows overwhelming advantages over traditional platinum and other hydrogel electrodes, hitherto reported in the literature. More importantly, the HPM-1 electrode was successfully demonstrated for optogenetic neuromodulation and simultaneously recording the brain's neural signals for 8 weeks. It is the first time to report the correlation between brain neural signals in the primary motor cortex region and corresponding limb behavior manipulated by light stimuli. The successful application benefits from the intrinsic features of the hydrogel including high transparency and excellent conductivity. This research shows significant progress in the design concept for implantable probes and substantively leapfrogs research advances toward the long-term goal of decoding brain neural information and understanding signal transmission through biohybrid interfaces, thereby opening new opportunities in the emerging study of human–machine interaction.

### Supporting Information

Supporting Information is available from the Wiley Online Library or from the author.

### Acknowledgements

The authors gratefully acknowledge the funding from the Jilin Province Science and Technology Development Plan (20210509036RQ and 2021SYHZ0038), the National Key Research and Development Program of China (2018YFD1100503 and 2020YFA0713601), the National Natural Science Foundation of China (U22A20183), and the Changchun Province Science and Technology Development Plan (21ZGY04). The wearable tests were approved by the Institutional Ethics Committee of the First Hospital of Jilin University (approval number 2021059, Changchun, China) with the consent of all volunteers and were carried out according to the relevant institutional guidelines and laws. The animal tests were approved by the Animal Ethics Committee of Changchun Institute of Applied Chemistry, Chinese Academy of Sciences (approval number 20220088, Changchun, China) and were carried out according to the relevant institutional guidelines and laws.

Note: The funding acknowledgements were corrected on March 2, 2023, after initial publication online.

### Conflict of Interest

The authors declare no conflict of interest.

### Data Availability Statement

Research data are not shared.

### Keywords

brain neural signals, conductive hydrogels, human–machine interfaces, implantable sensors, wearable sensors

Received: November 29, 2022  
Published online: January 3, 2023

- [1] W. Li, J. Jin, T. Xiong, P. Yu, L. Mao, *Angew. Chem., Int. Ed.* **2022**, *61*, e202204134.
- [2] R. e. Gilron, S. Little, R. Perrone, R. Wilt, C. de Hemptinne, M. S. Yaroshinsky, C. A. Racine, S. S. Wang, J. L. Ostrem, P. S. Larson, D. D. Wang, N. B. Galifianakis, I. O. Bledsoe, M. S. Luciano, H. E. Dawes, G. A. Worrell, V. Kremen, D. A. Borton, T. Denison, P. A. Starr, *Nat. Biotechnol.* **2021**, *39*, 1078.
- [3] T. A. Spix, S. Nanivadekar, N. Toong, I. M. Kaplow, B. R. Isett, Y. Goksen, A. R. Pfenning, A. H. Gittis, *Science* **2021**, *374*, 201.
- [4] K. W. Scangos, G. S. Makhoul, L. P. Sugrue, E. F. Chang, A. D. Krystal, *Nat. Med.* **2021**, *27*, 229.
- [5] J. K. Krauss, N. Lipsman, T. Aziz, A. Boutet, P. Brown, J. W. Chang, B. Davidson, W. M. Grill, M. I. Hariz, A. Horn, M. Schulder, A. Mammis, P. A. Tass, J. Volkmann, A. M. Lozano, *Nat. Rev. Neurol.* **2021**, *17*, 75.
- [6] Y. Cho, S. Park, J. Lee, K. J. Yu, *Adv. Mater.* **2021**, *33*, 2005786.
- [7] S. M. Won, E. Song, J. T. Reeder, J. A. Rogers, *Cell* **2020**, *181*, 115.
- [8] Y. Yang, S. Qiao, O. G. Sani, J. I. Sedillo, B. Ferrentino, B. Pesaran, M. M. Shanechi, *Nat. Biomed. Eng.* **2021**, *5*, 324.
- [9] W. Luo, D. Yun, Y. Hu, M. Tian, J. Yang, Y. Xu, Y. Tang, Y. Zhan, H. Xie, J. Guan, *Nat. Commun.* **2022**, *13*, 1601.
- [10] A. Serino, M. Bockbrader, T. Bertoni, S. ColachisIV, M. Solcà, C. Dunlap, K. Eipel, P. Ganzer, N. Annetta, G. Sharma, P. Orepic, D. Friedenberg, P. Sederberg, N. Faivre, A. Rezai, O. Blanke, *Nat. Hum. Behav.* **2022**, *6*, 565.
- [11] T. Xu, W. Ji, X. Wang, Y. Zhang, H. Zeng, L. Mao, M. Zhang, *Angew. Chem., Int. Ed.* **2022**, *61*, e202115074.
- [12] Q. Yang, T. Wei, R. T. Yin, M. Wu, Y. Xu, J. Koo, Y. S. Choi, Z. Xie, S. W. Chen, I. Kandela, S. Yao, Y. Deng, R. Avila, T. Liu, W. Bai, Y. Yang, M. Han, Q. Zhang, C. R. Haney, K. B. Lee, K. Aras, T. Wang, M. Seo, H. Luan, S. M. Lee, A. Brikha, N. Ghoreishi-Haack, L. Tran, I. Stepien, F. Aird, et al., *Nat. Mater.* **2021**, *20*, 1559.
- [13] M. Aime, N. Calcini, M. Borsa, T. Campelo, T. Rusterholz, A. Sattin, T. Fellin, A. Adamantidis, *Science* **2022**, *376*, 724.
- [14] W. Peng, Z. Wu, K. Song, S. Zhang, Y. Li, M. Xu, *Science* **2020**, *369*, eabb0556.
- [15] R. Chen, F. Gore, Q. Nguyen, C. Ramakrishnan, S. Patel, S. H. Kim, M. Raffee, Y. S. Kim, B. Hsueh, E. Krook-Magnusson, I. Soltesz, K. Deisseroth, *Nat. Biotechnol.* **2021**, *39*, 161.
- [16] Y. Li, L. Simmler, R. VanZessen, J. Flakowski, J. Wan, F. Deng, Y. Li, K. Nautiyal, V. Pascoli, C. Lüscher, *Science* **2021**, *373*, 1252.
- [17] Y. Yang, M. Wu, A. Vázquez-Guardado, A. J. Wegener, J. G. Grajales-Reyes, Y. Deng, T. Wang, R. Avila, J. A. Moreno, S. Minkowicz, V. Dumrongprechachan, J. Lee, S. Zhang, A. A. Legaria, Y. Ma, S. Mehta, D. Franklin, L. Hartman, W. Bai, M. Han, H. Zhao, W. Lu, Y. Yu, X. Sheng, A. Banks, X. Yu, Z. R. Donaldson, R. W. Gereau, C. H. Good, Z. Xie, et al., *Nat. Neurosci.* **2021**, *24*, 1035.
- [18] S. M. Won, L. Cai, P. Gutruf, J. A. Rogers, *Nat. Biomed. Eng.* **2021**, <https://doi.org/10.1038/s41551-021-00683-3>.
- [19] Y. Jiang, Z. Zhang, Y. Wang, D. Li, C. Coen, E. Hwaun, G. Chen, H. Wu, D. Zhong, S. Niu, W. Wang, A. Saberi, J. Lai, Y. Wu, Y. Wang, A. A. Trotsyuk, K. Y. Loh, C. Shih, W. Xu, K. Liang, K. Zhang, Y. Bai, G. Gurusankar, W. Hu, W. Jia, Z. Cheng, R. H. Dauskardt, G. C. Gurtner, J. B.-H. Tok, K. Deisseroth, et al., *Science* **2022**, *375*, 1411.
- [20] J. Li, Y. Liu, L. Yuan, B. Zhang, E. S. Bishop, K. Wang, J. Tang, Y. Zheng, W. Xu, S. Niu, L. Beker, T. L. Li, G. Chen, M. Diyaolu, A. Thomas, V. Mottini, J. B.-H. Tok, J. C. Y. Dunn, B. Cui, S. P. Paşca, Y. Cui, A. Habtezion, X. Chen, Z. Bao, *Nature* **2022**, *606*, 94.
- [21] L. Gao, J. Wang, Y. Zhao, H. Li, M. Liu, J. Ding, H. Tian, S. Guan, Y. Fang, *Adv. Mater.* **2022**, *34*, 2107343.
- [22] L. Zou, H. Tian, S. Guan, J. Ding, L. Gao, J. Wang, Y. Fang, *Nat. Commun.* **2021**, *12*, 5871.
- [23] N. Obidin, F. Tasnim, C. Dagdeviren, *Adv. Mater.* **2020**, *32*, 1901482.
- [24] M. Zhu, H. Wang, S. Li, X. Liang, M. Zhang, X. Dai, Y. Zhang, *Adv. Healthcare Mater.* **2021**, *10*, 2100646.
- [25] J. Shi, Y. Fang, *Adv. Mater.* **2019**, *31*, 1804895.
- [26] R. Chen, A. Canales, P. Anikeeva, *Nat. Rev. Mater.* **2017**, *2*, 10693.
- [27] A. Zátanyi, M. Madarász, Á. Szabó, T. Lőrincz, R. Hodován, B. Rózsa, Z. Fekete, *J. Neural Eng.* **2020**, *17*, 016062.
- [28] M. Thunemann, Y. Lu, X. Liu, K. Kılıç, M. Desjardins, M. Vandenberghe, S. Sadegh, P. A. Saisan, Q. Cheng, K. L. Weldy, H. Lyu, S. Djurovic, O. A. Andreassen, A. M. Dale, A. Devor, D. Kuzum, *Nat. Commun.* **2018**, *9*, 2035.
- [29] H. Shin, Y. Son, U. Chae, J. Kim, N. Choi, H. J. Lee, J. Woo, Y. Cho, S. H. Yang, C. J. Lee, I. Cho, *Nat. Commun.* **2019**, *10*, 3777.
- [30] S. Ward, C. Riley, E. M. Carey, J. Nguyen, S. Esener, A. Nimmerjahn, D. J. Sirbuly, *Nat. Commun.* **2022**, *13*, 3286.
- [31] X. Liu, C. Ren, Y. Lu, Y. Liu, J. Kim, S. Leutgeb, T. Komiyama, D. Kuzum, *Nat. Neurosci.* **2021**, *24*, 886.
- [32] D. Won, J. Kim, J. Choi, H. Kim, S. Han, I. Ha, J. Bang, K. K. Kim, Y. Lee, T. Kim, J. Park, C. Kim, S. H. Ko, *Sci. Adv.* **2022**, *8*, eabo3209.
- [33] G. Hong, C. M. Lieber, *Nat. Rev. Neurosci.* **2019**, *20*, 330.
- [34] J. Deng, H. Yuk, J. Wu, C. E. Varela, X. Chen, E. T. Roche, C. F. Guo, X. Zhao, *Nat. Mater.* **2021**, *20*, 229.
- [35] S. Park, H. Yuk, R. Zhao, Y. S. Yim, E. W. Woldegebriel, J. Kang, A. Canales, Y. Fink, G. B. Choi, X. Zhao, P. Anikeeva, *Nat. Commun.* **2021**, *12*, 3435.
- [36] D. O. Adewole, L. A. Struzyna, J. C. Burrell, J. P. Harris, A. D. Nemes, D. Petrov, R. H. Kraft, H. I. Chen, M. D. Serruya, J. A. Wolf, D. K. Cullen, *Sci. Adv.* **2021**, *7*, eaay5347.
- [37] Y. Cui, F. Zhang, G. Chen, L. Yao, N. Zhang, Z. Liu, Q. Li, F. Zhang, Z. Cui, K. Zhang, P. Li, Y. Cheng, S. Zhang, X. Chen, *Adv. Mater.* **2021**, *33*, 2100221.
- [38] G. Li, C. Li, G. Li, D. Yu, Z. Song, H. Wang, X. Liu, H. Liu, W. Liu, *Small* **2022**, *18*, 2101518.
- [39] M. A. Abed, H. B. Bohidar, *Eur. Polym. J.* **2005**, *41*, 2395.
- [40] H. Yan, Y. Wang, W. Shen, F. Li, G. Gao, T. Zheng, Z. Xu, S. Qian, C. Chen, C. Zhang, G. Yang, T. Chen, *Adv. Funct. Mater.* **2022**, *32*, 2203241.
- [41] G. Li, K. Huang, J. Deng, M. Guo, M. Cai, Y. Zhang, C. F. Guo, *Adv. Mater.* **2022**, *34*, 2200261.
- [42] X. Lu, Y. Si, S. Zhang, J. Yu, B. Ding, *Adv. Funct. Mater.* **2021**, *31*, 2103117.
- [43] Y. Lu, Y. Yue, Q. Ding, C. Mei, X. Xu, Q. Wu, H. Xiao, J. Han, *ACS Appl. Mater. Interfaces* **2021**, *13*, 50281.
- [44] H. Liu, C. Du, L. Liao, H. Zhang, H. Zhou, W. Zhou, T. Ren, Z. Sun, Y. Lu, Z. Nie, F. Xu, J. Zhu, W. Huang, *Nat. Commun.* **2022**, *13*, 3420.
- [45] H. Chen, J. Huang, J. Liu, J. Gu, J. Zhu, B. Huang, J. Bai, J. Guo, X. Yang, L. Guan, *J. Mater. Chem. A* **2021**, *9*, 23243.
- [46] J. Ren, Y. Liu, Z. Wang, S. Chen, Y. Ma, H. Wei, S. Lü, *Adv. Funct. Mater.* **2022**, *32*, 2107404.
- [47] X. Sun, S. He, M. Yao, X. Wu, H. Zhang, F. Yao, J. Li, *J. Mater. Chem. C* **2021**, *9*, 1880.
- [48] Z. He, W. Yuan, *ACS Appl. Mater. Interfaces* **2021**, *13*, 1474.
- [49] J. Yu, M. Wang, C. Dang, C. Zhang, X. Feng, G. Chen, Z. Huang, H. Qi, H. Liu, J. Kang, *J. Mater. Chem. C* **2021**, *9*, 3635.
- [50] J. Lu, J. Gu, O. Hu, Y. Fu, D. Ye, X. Zhang, Y. Zheng, L. Hou, H. Liu, X. Jiang, *J. Mater. Chem. A* **2021**, *9*, 18406.
- [51] J. Hu, T. Kurokawa, T. Nakajima, Z. L. Wu, S. M. Liang, J. P. Gong, *Macromolecules* **2014**, *47*, 3587.
- [52] C. Zhang, Y. Zhou, H. Han, H. Zheng, W. Xu, Z. Wang, *ACS Nano* **2021**, *15*, 1785.
- [53] X. Chen, M. He, X. Zhang, T. Lu, W. Hao, Y. Zhao, Y. Liu, *Macromol. Chem. Phys.* **2020**, *221*, 2000054.
- [54] L. Chen, X. Chang, J. Chen, Y. Zhu, *ACS Appl. Mater. Interfaces* **2022**, *14*, 43833.
- [55] Y. Li, C. Liu, X. Lv, S. Sun, *Soft Matter* **2021**, *17*, 2142.
- [56] F. He, X. You, H. Gong, Y. Yang, T. Bai, W. Wang, W. Guo, X. Liu, M. Ye, *ACS Appl. Mater. Interfaces* **2020**, *12*, 6442.

- [57] L. Zhang, K. S. Kumar, H. He, C. J. Cai, X. He, H. Gao, S. Yue, C. Li, R. C. Seet, H. Ren, J. Ouyang, *Nat. Commun.* **2020**, *11*, 4683.
- [58] Z. Lu, S. Xu, H. Wang, E. He, J. Liu, Y. Dai, J. Xie, Y. Song, Y. Wang, Y. Wang, L. Qu, X. Cai, *ACS Appl. Bio. Mater.* **2021**, *4*, 4872.
- [59] Y. Wang, Z. Feng, J. Wang, X. Zheng, *Neural Regener. Res.* **2014**, *9*, 1138.
- [60] G. Girardeau, V. Lopes-Dos-Santos, *Science* **2021**, *374*, 560.
- [61] A. Bergel, T. Deffieux, C. Demené, M. Tanter, I. Cohen, *Nat. Commun.* **2018**, *9*, 5364.
- [62] J. Orzeł-Gryglewska, P. Matulewicz, E. Jurkowlaniec, *Behav. Brain Res.* **2014**, *265*, 84.
- [63] H. Sheng, X. Wang, N. Kong, W. Xi, H. Yang, X. Wu, K. Wu, C. Li, J. Hu, J. Tang, J. Zhou, S. Duan, H. Wang, Z. Suo, *Extreme Mech. Lett.* **2019**, *30*, 100510.
- [64] V. S. Polikov, P. A. Tresco, W. M. Reichert, *J. Neurosci. Methods* **2005**, *148*, 1.
- [65] M. P. Ward, P. Rajdev, C. Ellison, P. P. Irazoqui, *Brain Res.* **2009**, *1282*, 183.
- [66] A. H. All, X. Zeng, D. B. L. Teh, Z. Yi, A. Prasad, T. Ishizuka, N. Thakor, Y. Hiromu, X. Liu, *Adv. Mater.* **2019**, *31*, 1803474.
- [67] M. Choi, M. Humar, S. Kim, S.-H. Yun, *Adv. Mater.* **2015**, *27*, 4081.
- [68] Y. U. Cho, J. Y. Lee, U. Jeong, S. H. Park, S. L. Lim, K. Y. Kim, J. W. Jang, J. H. Park, H. W. Kim, H. Shin, H. J. Jeon, Y. M. Jung, I. Cho, K. J. Yu, *Adv. Funct. Mater.* **2022**, *32*, 2105568.
- [69] R. Toosi, M. A. Akhaee, M. A. Dehaqani, *Sci. Rep.* **2021**, *11*, 13925.